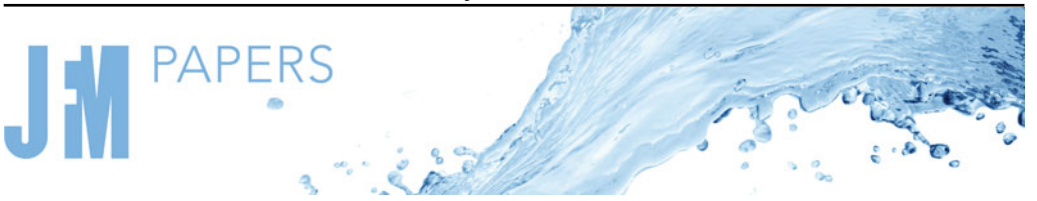
J. Fluid Mech. (2025), *vol.* 1019, A43, doi:10.1017/jfm.2025.10580



Aeroacoustics of vortex–wedge interaction

Marios I. Spiropoulos[1], **Florent Margnat**[1], **Vincent Valeau**[1] **and Peter Jordan**[1]

[1]Institute PPRIME UPR, 3346, CNRS – University of Poitiers – ENSMA, 86022 Poitiers, France

Corresponding author: Marios I. Spiropoulos; Email: marios-ioannis.spiropoulos@ensma.fr

(Received 7 April 2025; revised 30 June 2025; accepted 22 July 2025)

We consider the vortex–wedge interaction problem, taking as a departure point Howe's model of a point vortex interacting with a semi-infinite half-plane, where the vortex path is influenced by its image and a closed-form analytical solution is obtained for the sound field. We generalise Howe's model to consider wedges of arbitrary angles and explore the influence of vortex circulation, distance from the edge and the wedge half-angle. The effect of wedge angle on sound emission involves a reduced amplitude of the latter as the former is increased. An extension of the model is proposed to account for convection effects by a non-zero ambient flow. We identify a non-dimensional parameter that characterises the vortex kinematics close to the edge and the associated acoustic effect: high and low values of the parameter correspond, respectively, to high- and low-amplitude sound emission of high and low frequency.

Key words: aeroacoustics, hydrodynamic noise, flow-structure interactions

1. Introduction

Sound generated by the interaction of turbulent flows with edges is prevalent in many industrial applications: side-edge noise of flaps (Hardin 1980; Guo 2011), airfoil-noise (Howe 2001; Roger & Moreau 2005; Moreau & Roger 2009; Lee *et al.* 2021), jet-flap interaction noise (Cavalieri *et al.* 2014; Jordan *et al.* 2018; Huber *et al.* 2024) and whistling of side-view mirrors (Stoffel *et al.* 2025), to cite just a few examples. The problem of trailing-edge noise has, in particular, received much attention and there is a substantial number of associated theoretical and experimental studies. Hybrid numerical approaches have been proposed where the flow field containing the sound sources is obtained by unsteady Reynolds-averaged Navier–Stokes simulations, large-eddy simulations or direct numerical simulations and the sound in the far-field computed using acoustic analogies and the tailored Green functions (Wang 2000). The first review on trailing edge noise was conducted by Howe (1978) who considered theoretical developments, while detailed

© The Author(s), 2025. Published by Cambridge University Press.

https://doi.org/10.1017/jfm.2025.10580 Published online by Cambridge University Press

reviews on the subject can be found in the works of Doolan & Moreau (2015) for experimental studies with applications to wind-turbine noise and Lee *et al.* (2021) for a more global classification of numerical, experimental and theoretical approaches on trailing-edge noise and its control.

Theoretical models based on Lighthill's acoustic analogy (Lighthill 1952) and the works of Curle (1955) and Ffowcs Williams & Hawkings (1969) or the theory of vortex sound (Powell 1964; Howe 1975*a*) can shed light on the mechanism of aerodynamic noise generation for wall-bounded flows and many of these have been used for the problem of airfoil noise. The sound due to the interaction of a flow with geometrical objects is mostly generated at the edges (Roger, Moreau & Kucukcoskun 2016). The scattering properties of geometries are often taken into account by considering the edges as semi-infinite half-planes or wedges, for which exact (Macdonald 1915; Biot & Tolstoy 1957) and approximate analytical solutions (Menounou & Nikolaou 2017; Menounou, Spiropoulos & Nikolaou 2023) exist, and the flow-structures interacting with the object are frequently accounted for via a sound-source term crafted according to the acoustic analogy considered. Such approaches have led to fundamental results for the aeroacoustics of turbulent flows interacting with edges. For instance, Ffowcs Williams & Hall (1970) applied Lighthill's theory to show that compact quadrupole sources close to the edge of a semi-infinite half-plane lead to an acoustic intensity that scales with the fifth power of the turbulent velocity. Crighton & Leppington (1971) calculated scaling laws for acoustically compact quadrupole and dipole sources for soft and hard wedge-like objects by considering that the Green function can be obtained as a solution of the Laplace equation when the observer is many wavelengths away and the object is acoustically compact. Crighton (1972) examined the aerodynamic sound generated by a line vortex with its axis parallel to the edge of a semi-infinite rigid half-plane. Howe (Howe 1975*a*,*b*), by introducing the concept of the compact Green functions, extended this idea to two-dimensional (2-D) problems in the time domain and obtained simple closed-form analytical solutions that clarify the physical mechanisms underpinning aerodynamic sound generation (Howe 1998, 2003). Priddin *et al.* (2018) illustrated how simplified models derived in that framework can be used to investigate methods of passive and active control of the trailing edge noise. The aeroacoustics of the half-plane/vortex system was also studied by Kambe, Minota & Ikushima (1985) who performed a theoretical and experimental study, considering that the vortex kinematics are entirely governed by free stream convection. Their theoretical model was then extended to wedges of arbitrary angles by Chang & Chen (1994) and to porous half-planes by Chen *et al.* (2022). Despite the fact that previous works have treated the problem of sound generation by vortex–wedge interactions (Crighton & Leppington 1970; Chang & Chen 1994) and resulted in useful scaling laws, to the best of the authors' knowledge, no explicit closed form, analytical formulae are presented that describe the sound field produced when a vortex induced by its image follows a trajectory in the vicinity of a semi-infinite rigid wedge. Furthermore, most of the models related to point vortex–edge interactions consider either that the point vortex is purely convected by a free stream (Kambe *et al.* 1985; Chang & Chen 1994; Chen *et al.* 2022) or its path is solely influenced by its image as in the works of Crighton (1972) and Howe (2003). Kambe *et al.* (1985) and more recently Chen *et al.* (2022) mentioned that the path of a convected vortex ring alters its trajectory when passing in the vicinity of a half-plane and this path-deviation depends on the vortex circulation. However, a more detailed investigation on the competing mechanisms of convection and edge effects on the vortex path and sound field was not carried out.

In the present work, we propose a generalisation of Howe's vortex half-plane interaction problem, by deriving closed-form analytical solutions in both time and frequency domains,

https://doi.org/10.1017/jfm.2025.10580 Published online by Cambridge University Press

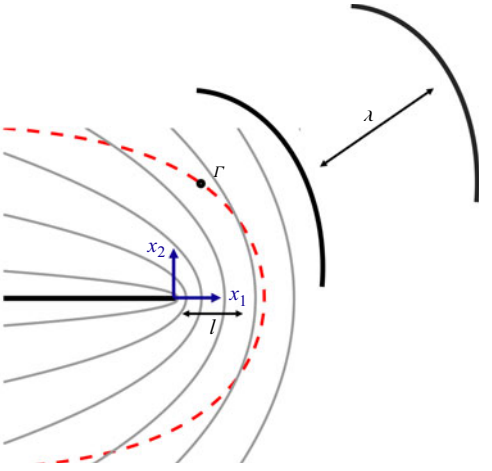


Figure 1. Acoustic waves with wavelength λ generated by the 2-D interaction between a point vortex (black dot) with circulation Γ and a semi-infinite, rigid half-plane. The red-dashed line corresponds to the vortex trajectory due to the interaction with its image point and the grey solid lines to the streamlines of the incompressible potential around the edge. Here l is the minimum distance between the vortex and the edge ($l \ll \lambda$).

when a point vortex is induced around the edge of a semi-infinite rigid wedge. The model is then extended to include the combined effects of vortex induction and convection by a non-zero ambient flow.

The paper is structured as follows. In § 2, Howe's model is briefly recalled while its extension to arbitrary wedge-angles is proposed in § 3 in frequency- and time-domains. The combined effect of convection and induction is considered in § 4 and in § 5 we conclude the paper and include a discussion regarding possible applications of the model for aeroacoustic problems such as noise generation by the trailing edges of airfoils.

2. Vortex–edge interaction: Howe's half-plane problem

A generic turbulent fluctuation in the vicinity of the edge of a semi-infinite rigid plate ($x_1 < 0$, $x_2 = 0$) is modelled as a point vortex, shown in figure 1. It is assumed that the acoustic wavelength λ is much larger than the smallest distance l between the edge and the vortex. Any effect of the free stream flow is omitted and the trajectory of the point vortex is influenced only by its image. Howe's theory of vortex sound is applied to obtain the pressure pulse in the far field,

$$p\,(\boldsymbol{x},\,\tau) = -\rho \int_V \int_{-\infty}^{\infty} (\boldsymbol{\omega} \times \boldsymbol{v})\,(\boldsymbol{y},\,t)\,\boldsymbol{\nabla} G\,(\boldsymbol{x},\,\boldsymbol{y},\,t-\tau)\,\mathrm{d}t\mathrm{d}^3\boldsymbol{y}, \tag{2.1}$$

where G denotes the tailored Green function for the half-plane, ρ the medium's density (assumed to be constant), $\boldsymbol{\nabla} = (\partial/\partial y_1,\, \partial/\partial y_2,\, \partial/\partial y_3)$ the del operator and $\boldsymbol{\omega}$, $\boldsymbol{v}$ are the vorticity and velocity fields, respectively.

For an observer in the acoustic far-field and a source located in the vicinity of the edge of the half-plane ($kl \equiv 2\pi l/\lambda \ll 1$), Howe used an asymptotic expression of the half-plane Green function to compute the scattered sound field (Howe 1975*a*, 1998). An integration along the span is performed to reduce the problem to two dimensions and the resulting low-frequency, 2-D Green function is obtained using the method of stationary phase. The time-domain compact Green function for the diffraction field around a half-plane is obtained by taking the inverse Fourier transform of its frequency domain counterpart and reads as

https://doi.org/10.1017/jfm.2025.10580 Published online by Cambridge University Press

(details in the appendix of the work of Howe 1975*a*)

$$G(\boldsymbol{x},\, \boldsymbol{y}, t-\tau) \approx \frac{\phi^*(\boldsymbol{x})\phi^*(\boldsymbol{y})}{\pi|\boldsymbol{x}|}\delta\,(t-\tau),\ |\boldsymbol{x}| \to \infty, \tag{2.2}$$

where $\boldsymbol{x} = (x_1, x_2)$ denotes the coordinates of the observer in the far field, such that $k|\boldsymbol{x}| \gg 1$ and $\boldsymbol{y} = (y_1, y_2)$ correspond to the source/vortex coordinates and $\delta(\cdot)$ is the Dirac delta function. The origin (0, 0) coincides with the edge of the half-plane (figure 1) and the position vector of the vortex is denoted as $\boldsymbol{y}_0$, such that $k|\boldsymbol{y}_0| \ll 1$. Here $\tau = t - |\boldsymbol{x}|/c_0$ is the retarded time, c_0 the speed of sound and $\phi^*(\cdot)$ is the incompressible velocity potential of the flow around the edge of the half-plane, which is used to compute the low-frequency Green function in the limit of $k|\boldsymbol{y}| \ll 1$. Note that $\phi^*(\cdot)$ is not related to the actual flow field, it is rather a mathematical tool to obtain the Green function, denoted by Howe (2003) as a hypothetical velocity potential.

For a point vortex, the source term can be written as (Howe 1975*a*)

$$\boldsymbol{\omega} \times \boldsymbol{v} = \Gamma \boldsymbol{e}_3 \times \frac{\mathrm{d}\boldsymbol{y}}{\mathrm{d}t}\delta(\boldsymbol{y} - \boldsymbol{y}_0(t)), \tag{2.3}$$

where Γ is the circulation of the vortex. From here on, the polar coordinate system will be used: (i) $\boldsymbol{x} = r(\cos\theta, \sin\theta)$ and (ii) $\boldsymbol{y}_0 = r_0(\cos\theta_0, \sin\theta_0)$, unless stated otherwise. Substituting (2.2), (2.3) into (2.1) the pressure pulse in the far field can be written in the form

$$p(\boldsymbol{x}, \tau) = \frac{\rho\Gamma \sin(\theta/2)}{\pi\sqrt{r}}\left[\frac{\mathrm{d}\boldsymbol{y}_0}{\mathrm{d}\tau} \cdot \nabla\Psi^*\right](\boldsymbol{y}_0), \tag{2.4}$$

where Ψ^* is the stream function associated with the velocity potential ($\phi^*(\boldsymbol{y}_0)$) near the edge of the half-plane. With the operator $\mathrm{D}/\mathrm{D}\tau$ corresponding to the material derivative with respect to the vortex trajectory for 2-D flow, we can write (Cartesian coordinates for simplicity) (Howe 2003)

$$\frac{\mathrm{d}\boldsymbol{y}_0}{\mathrm{d}\tau} \cdot \nabla\Psi^* = \frac{\mathrm{d}y_{01}}{\mathrm{d}\tau}\frac{\mathrm{d}\Psi^*}{\mathrm{d}y_{01}} + \frac{\mathrm{d}y_{02}}{\mathrm{d}\tau}\frac{\mathrm{d}\Psi^*}{\mathrm{d}y_{02}} = \frac{\mathrm{D}\Psi^*}{\mathrm{D}\tau}(\boldsymbol{y}_0). \tag{2.5}$$

One of the key results of this simplified model is the following physical interpretation it enables regarding the mechanism of sound generation. The far-field sound is generated when the vortex path crosses the streamlines, given by Ψ^*. Vortices that follow these streamlines do not produce sound. In particular, a vortex far from the edge, translating parallel to the half-plane (and hence the streamlines Ψ^*) with an equivalent velocity $v = \Gamma/(8\pi l)$ is silent (Howe 1975*a*, 1998, 2003).

The material derivative $\mathrm{D}\Psi^*/\mathrm{D}\tau$ depends on the vortex path, which is obtained by taking into account the vortex and its image, details shown in Howe (2003). This provides an expression for the acoustic pressure as a function of vortex circulation and smallest vortex-edge distance,

$$p(\boldsymbol{x}, \tau, l, \Gamma) = \frac{\rho\Gamma^2 \sin(\theta/2)}{(4\pi l)^2}\sqrt{\frac{l}{r}}\left[\frac{\Gamma\tau/\left(8\pi l^2\right)}{\left[1 + \left(\Gamma\tau/\left(8\pi l^2\right)\right)^2\right]^{5/4}}\right]. \tag{2.6}$$

Kambe *et al.* (1985) studied a similar problem theoretically, where a thin vortex ring interacts with a sharp edge. The problem was treated in three-dimensions by applying the theory of vortex sound and using the inverse-Fourier-transformed asymptotic low-frequency forms of the half-plane Green function. In their analysis the vortex does not

https://doi.org/10.1017/jfm.2025.10580 Published online by Cambridge University Press

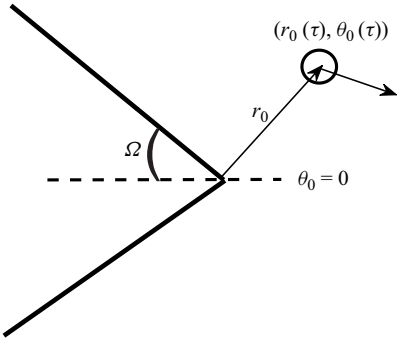


Figure 2. Geometry of the wedge problem.

interact with its image and is considered to pass by the edge without altering its trajectory. Kambe *et al.* validated their result experimentally, showing that it is the rate-of-change of a volume flux of a hypothetical potential flow around the edge that leads to sound generation. Chang & Chen (1994) later followed the same methodology and used an asymptotic, low-frequency form of the Green function for a semi-infinite rigid wedge to extend Kambe's model to semi-infinite sharp wedges, including the half-plane as a special case.

Notice that in the works of Crighton (1972) and Howe (1975*b*) the problem of sound generation by vortex half-plane interactions is considered in two dimensions, where Howe has shown that sound is generated due to the crossing of the vortex through the hypothetical streamlines. The works of Kambe *et al.* (1985) for half-planes and Chang & Chen (1994) for wedges extend Howe's model to three dimensions and hence they conclude that the sound is generated due to the rate-of-change of the volume flux of the hypothetical potential flow when a vortex ring crosses its streamlines. It is thus seen that the physical mechanism of sound generation is similar, however, both models consider different vortex kinematics. On the one hand (Howe's model) the point vortex is self-induced around the edge of the half-plane, while the models of Kambe and Chang–Chen consider that the vortex ring moves on a straight line and its trajectory is not affected by the edge. In the following sections we are going to focus on the 2-D problem (Howe's model) and extend it to consider (i) wedges of arbitrary angles and (ii) the combined effect of convection and self-induction in the vortex kinematics.

3. Extension to the semi-infinite rigid wedge

In what follows, the analysis of Howe for the 2-D problem of a point vortex interacting with a half-plane is generalised for any arbitrary wedge with half-angle Ω. Explicit formulae for the acoustic pressure are given in both frequency and time domains while extension of the model to account for non-zero convection velocity and the associated edge-effect on vortex kinematics and sound will be considered in a subsequent section.

Figure 2 shows the configuration considered. The wedge parameter $\gamma = 2(\pi - \Omega)/\pi$ is introduced and ranges from $\gamma = 2$, which corresponds to the limiting case of a semi-infinite half-plane, to $\gamma = 1$ (infinite wall). The physical space is restricted from the lower to the upper face of the wedge, $\theta_0 \in [-\gamma\pi/2, \gamma\pi/2]$. Note that for $\gamma < 1$ the problem resembles rather the aerodynamic sound generated by a closed triangular cavity, which is beyond the scope of the present study. Following Howe's methodology (Howe 2003), the complex velocity potential close to the edge is given by

$$W(z_j) = -iz_j^{1/\gamma} = -ir_j^{1/\gamma}\left(\cos(\theta_j/\gamma) + i\sin(\theta_j/\gamma)\right), \tag{3.1}$$

https://doi.org/10.1017/jfm.2025.10580 Published online by Cambridge University Press

where $z_j = r_j e^{i\theta_j}$ and r_j, θ_j denote source or receiver coordinates, $\phi^* = \mathrm{Re}[-iW(z_j)]$ and $\Psi^* = \mathrm{Im}[-iW(z_j)]$ (Howe 2003). Combining (2.1), (2.2), (2.3) and (3.1) one obtains

$$p\,(r, \theta, \tau, \Gamma, l, \gamma) = \frac{\rho\Gamma \sin(\theta/\gamma)}{\pi r^{\frac{\gamma-1}{\gamma}}}\left[-\frac{r_0^{1/\gamma-1}(\tau)}{\gamma}\frac{\mathrm{d}r_0}{\mathrm{d}\tau}(\tau)\cos\left(\frac{\theta_0(\tau)}{\gamma}\right) + \frac{r_0^{1/\gamma}(\tau)}{\gamma}\sin\left(\frac{\theta_0(\tau)}{\gamma}\right)\frac{\mathrm{d}\theta_0}{\mathrm{d}\tau}(\tau)\right], \tag{3.2}$$

where the position of the vortex in polar coordinates $r_0(\tau)$, $\theta_0(\tau)$ is given as a function of the retarded time τ.

3.1. *Self-induction around a semi-infinite rigid wedge*

A single point vortex is first considered in the vicinity of the corner of a semi-infinite wedge and for zero free stream velocity. The equations of motion are obtained by the following expression (Howe 2003):

$$\frac{\mathrm{d}z_0^*}{\mathrm{d}t} = -i\frac{\Gamma\zeta''(z_0)}{4\pi\zeta'(z_0)} + F'(z_0), \tag{3.3}$$

where z_0 is the position of the vortex core in the complex plane, z_0^* is the complex conjugate of z_0, $\zeta(z_0)$ is the conformal mapping of z_0 in the ζ-plane and $F(z_0)$ is a regular function of z_0. The symbols $(')$, $('')$ denote the first and second derivatives with respect to the complex variable z. Since the convection of the vortex core is not considered, we may write

$$F\,(z_0) = \frac{i\Gamma}{2\pi}\ln\left(\zeta(z) - \zeta^*(z_0)\right), \tag{3.4}$$

which corresponds to the velocity field induced by an image vortex. To account for the presence of a corner the following conformal transform is applied:

$$\zeta\,(z) = iz^{1/\gamma}. \tag{3.5}$$

Using the polar form of the complex number, $z = re^{i\theta}$, (3.3) results in a 2×2 system of nonlinear differential equations of first order. The vortex position at any time instant is then given by

$$\begin{aligned} r_0(\tilde{\tau}) &= l\sqrt{1 + (2\tilde{\tau}/\gamma)^2}, \\ \theta_0(\tilde{\tau}) &= \gamma\tan^{-1}(-2\tilde{\tau}/\gamma), \end{aligned} \tag{3.6}$$

where $\tilde{\tau} = \Gamma\tau/8\pi l^2$ is a non-dimensional time parameter and l denotes the smallest distance from the vortex to the edge and depends on the initial conditions as shown in the full steps of the derivation in Appendix A. Equation (3.6) implies that the kinematics of the vortex are purely driven by the circulation and the smallest distance to the edge l, since convection effects are neglected.

Substituting (3.6) into (3.2) we obtain an expression for the far-field pressure pulse, written as the product of two parameters, one (defined as C) which is constant and contains the amplitude and directivity and a second (defined as T_{wedge}) that depends on time and

https://doi.org/10.1017/jfm.2025.10580 Published online by Cambridge University Press

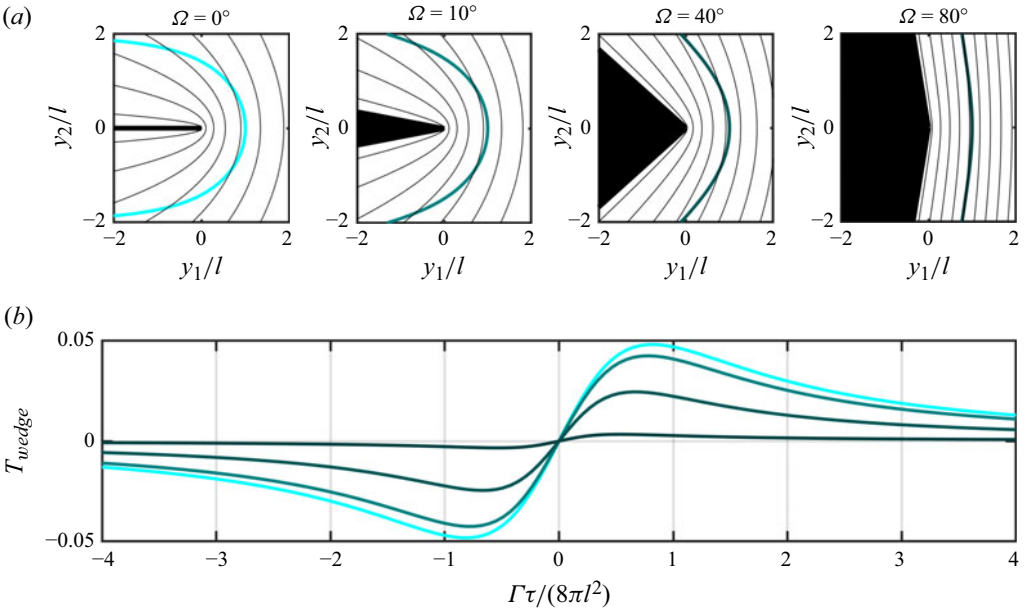


Figure 3. Vortex path (a) and normalised pressure pulses ($T_{wedge} = p/C$) (b), obtained for an observer at ($r = 20l$, $\theta = \pi/2$) for different wedge angles. The vortex arrives close to the edge with $v = 17\ \mathrm{m\,s^{-1}}$ and the closest distance from the edge is $l = 0.025$ m. The circulation of the vortex is computed as $\Gamma = v/8\pi l$. The black, solid lines correspond to the streamlines of the incompressible potential around the edge in the absence of vortices.

the wedge angle:

$$\begin{aligned} p\,(r, \theta, \tilde{\tau}, \Gamma, l, \gamma) &= C\,(\theta/\gamma, \Gamma, l)\, T_{wedge}\,(r, l, \tilde{\tau}, \gamma), \\ C\,(\theta/\gamma, \Gamma, l) &= \frac{\rho \Gamma^2}{8\pi^2 l^2} \sin(\theta/\gamma), \\ T_{wedge}\,(r, l, \tilde{\tau}, \gamma) &= 2\frac{(rl)^{1/\gamma}}{r}\left(\frac{\gamma - 1}{\gamma^2}\right)\left[\frac{2\tilde{\tau}/\gamma}{\left[1 + (2\tilde{\tau}/\gamma)^2\right]^{\frac{3\gamma-1}{2\gamma}}}\right]. \end{aligned} \tag{3.7}$$

Equation (3.7) is a generalisation of (2.6) for arbitrary wedge angles, $\gamma \in [2, 0)$. Indeed, for $\gamma = 2$ ($\Omega = 0$) (3.7) reduces to (2.6). It can be seen that the wedge angle influences the vortex path and thus the far-field pressure. In the limiting case of $\gamma = 1$ ($\Omega = \pi/2$) (infinite wall), the vortex path is parallel to the streamlines of the hypothetical potential flow and (3.7) yields $p = 0$. The pressure pulse is mainly dependent on the wedge time function $T_{wedge}(r, l, \tilde{\tau}, \gamma)$, since the amplitude is constant and the directivity function ($\sin(\theta/\gamma)$) takes values from -1 to 1. Figure 3 shows the vortex path and the hypothetical streamlines (figure 3a) while in figure 3(b) a comparison of the acoustic pulses for different wedge angles is shown. By examining the behaviour of the wedge time function, it can be shown that the maximum value of the pressure pulse depends explicitly on the wedge angle. The maxima are found by

$$\frac{\partial T_{wedge}}{\partial \tilde{\tau}} = 0, \tag{3.8}$$

https://doi.org/10.1017/jfm.2025.10580 Published online by Cambridge University Press

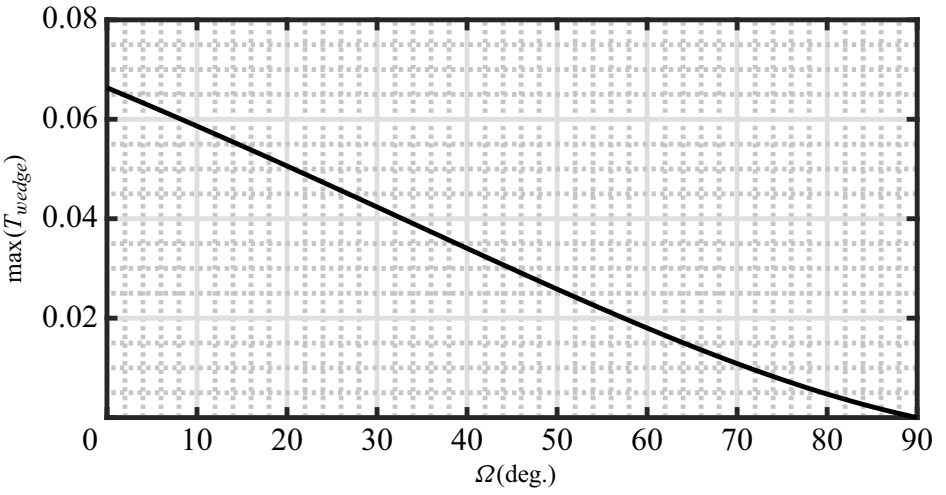


Figure 4. Maximum values of T_{wedge} with respect to the wedge angle, obtained by (3.10), for $l = 0.025$ m and $r = 20l$.

and the non-dimensional time for peak radiation is given by

$$\tilde{\tau}_{max} = (\gamma/2)\sqrt{\frac{\gamma}{2\gamma - 1}}. \tag{3.9}$$

The non-dimensional time $\tilde{\tau}_{max}$ decreases as the wedge angle increases, i.e. for vortices with the same circulation and distance from the edge, the radiation-peak that corresponds to an arbitrary wedge angle, for instance $\Omega = 40°$, happens sooner than the one of the half-plane as shown in figure 3.

Substituting (3.9) into (3.7), it follows that the maxima of the pressure pulse are obtained by

$$\max\left[T_{wedge}\right](r, l, \gamma) = 2\frac{(rl)^{1/\gamma}}{r}\left(\frac{\gamma - 1}{\gamma^2}\right)\left[\frac{\sqrt{\frac{\gamma}{2\gamma-1}}}{\left[1 + \frac{\gamma}{2\gamma-1}\right]^{\frac{3\gamma-1}{2\gamma}}}\right]. \tag{3.10}$$

Figure 4 depicts the trends of the maxima of the far field pressure pulses (3.10) for $\Omega \in [0, 90°]$. The model thus indicates a decrease of the peak sound-radiation amplitude as the wedge angle increases.

Examining (3.9) and solving for the dimensional time τ_{max} that corresponds to the maximum amplitude yields

$$\tau_{max} = \frac{4\pi l^2}{\Gamma}\gamma\sqrt{\frac{\gamma}{2\gamma - 1}}. \tag{3.11}$$

The time when the sound pulse reaches its maximum amplitude depends on (i) the circulation, (ii) the distance from the edge and (iii) the wedge angle. For sources closer to the edge and/or vortices with strong circulation, τ_{max} decreases and thus the peak radiation occurs sooner; corresponding to higher-frequency sound emission, while τ_{max} decreases as Ω increases, as discussed above for its non-dimensional counterpart.

https://doi.org/10.1017/jfm.2025.10580 Published online by Cambridge University Press

The asymptotic behaviour of the far field pressure for short non-dimensional times, that is $2\tilde{\tau}/\gamma \ll 1$ can be found as

$$p_{short} = \frac{(rl)^{1/\gamma}}{r}\frac{\rho\Gamma^2}{2\pi^2 l^2}\sin(\theta/\gamma)\left(\frac{\gamma-1}{\gamma^3}\right)\tilde{\tau}, \tag{3.12}$$

showing a linear dependence on $\tilde{\tau}$.

Considering a turbulent eddy modelled as a vortex of circulation $\Gamma = 2\pi v R$, where R the radius and v a measure of the velocity fluctuation, the time scale can be approximated as $\tau = l/v$. It follows that

$$\frac{2\Gamma\tau}{8\pi l^2\gamma} = \frac{1}{2\gamma}\left(\frac{R}{l}\right). \tag{3.13}$$

The asymptotic expression of (3.12) can be reformulated in order to derive the following scaling law:

$$p_{short} \sim v^2 l^{\frac{1-3\gamma}{\gamma}} R^3, \quad R/l \ll 1. \tag{3.14}$$

Kambe *et al.* (1985) showed experimentally that vortices passing near a semi-infinite plate, with $R/l \ll 1$ follow a scaling law $v^{2.53}l^{-2.24}$. For $\gamma = 2$ the asymptotic expression of (3.14) gives $p \sim v^2 l^{-2.5}$. However, in the general case (3.7) illustrates that the pressure scales as $\sim l^{(1-2\gamma)/\gamma}$, which agrees with the results of the scaling to a factor of $l^{-3/2}$ obtained by Ffowcs Williams & Hall (1970) for the infinite plate, when $\gamma = 2$.

3.2. *Extension to frequency domain*

The foregoing analysis can be extended to the frequency domain. The fact that the radiation peak occurs sooner for higher wedge angles indicates, as mentioned, that as Ω increases the acoustic energy is distributed to higher frequencies. This can be shown by considering the Fourier transform of (3.7), which has the following form (detailed derivations are shown in Appendix B):

$$\begin{aligned}\hat{p}(r,\theta,\tilde{\omega},l,\gamma) &= \tilde{C}(\theta/\gamma)\,\hat{T}_{wedge}(r,l,\tilde{\omega},\gamma),\\ \tilde{C}(\theta/\gamma) &= \rho\sin(\theta/\gamma),\end{aligned} \tag{3.15}$$

$$\hat{T}_{wedge}(r,l,\tilde{\omega},\gamma) = -i\frac{(rl)^{1/\gamma}}{r}\frac{4}{\gamma}\left(\frac{\gamma-1}{\gamma^2}\right)\left(\frac{4}{\gamma^2}\right)^{\frac{1}{2\gamma}-3/2}\frac{\sqrt{\pi}\left(\frac{\gamma^2}{2}\right)^{\frac{1}{2\gamma}}}{\tilde{\Gamma}\left(\frac{3}{2}-\frac{1}{2\gamma}\right)}\tilde{\omega}^{1-\frac{1}{2\gamma}}K_{\frac{1}{2\gamma}}\left(\frac{\gamma^2}{4}\tilde{\omega}\right),$$

where $\tilde{\Gamma}(\cdot)$ is the gamma function,

$$K_\nu(q) = \frac{i\pi}{2}e^{i\frac{\pi}{2}\nu}H_\nu^{(1)}\left(qe^{i\pi/2}\right) \tag{3.16}$$

is the modified Bessel function, q an arbitrary variable, $H_\nu^{(1)}(\cdot)$ the Hankel function of the first kind and

$$\tilde{\omega} = \frac{8\pi l^2}{\Gamma}\omega \tag{3.17}$$

https://doi.org/10.1017/jfm.2025.10580 Published online by Cambridge University Press

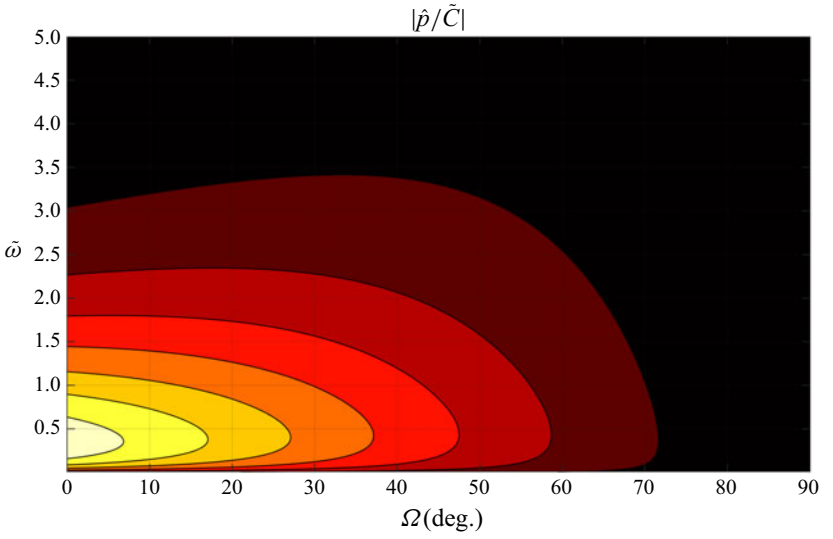


Figure 5. Amplitude of the acoustic pressure (3.15) generated by the vortex–wedge interaction as a function of the dimensionless frequency and the wedge angle. The results are shown for an observer located at $r = 20l$ and $l = 0.025$ m.

is the dimensionless frequency of the sound wave. The sound-wavelength associated with $\tilde{\omega}$ is

$$\frac{\lambda_\Gamma}{l} = \frac{1}{\tilde{\omega}} \frac{16\pi^2 l c_0}{\Gamma}. \tag{3.18}$$

Equation (3.18) is in agreement with the time-domain analysis of the problem, where high values of Γ and/or small values of l lead to acoustic waves with shorter wavelengths (higher frequencies), however, the frequency-domain analysis allows the derivation of an explicit relation between the acoustic wavelength and its dependence on the main parameters of the problem. Moreover, the analysis indicates that in a realistic turbulent flow around an edge, flow structures that remain close to the edge radiate at wavelengths (λ_Γ) that scale with the circulation and the distance from the edge.

Figure 5 shows the spectrum of $\hat{T}_{wedge}(r, l, \tilde{\omega}, \gamma) = \hat{p}/\tilde{C}$ (3.15) as a function of the wedge angle and the non-dimensional frequency. The sound energy for the half-plane ($\Omega = 0$ or $\gamma = 2$) is mostly concentrated at low non-dimensional frequencies, while with increasing wedge angle a slight broadening of the spectrum to higher frequencies is observed. However, as observed in the time-domain analysis, the amplitude of the acoustic pressure has maximum values for small wedge angles ($\Omega \to 0$) and the half-plane is the most acoustically efficient scatterer of all wedges, which is consistent with similar findings in the literature (Crighton & Leppington 1971; Chang & Chen 1994).

The foregoing is restricted to two-dimensions, low frequencies with turbulent flow-structures represented by point vortices that interact with their images inside the wedge. Despite these simplifications, which are justified since quasi-2-D structures have been shown to be the key sound-radiation structures for trailing edges in turbulent flow (Sano *et al.* 2019; Abreu *et al.* 2021; Demange *et al.* 2024*a*; Yuan *et al.* 2024), the model provides physical insight regarding the parameters that influence the acoustic-field generated by vorticity in the vicinity of edges with arbitrary angles. It was shown that the circulation (Γ) and the minimum distance (l) between the vortex and the edge influences the wavelength of the radiated sound waves as shown by (3.18).

https://doi.org/10.1017/jfm.2025.10580 Published online by Cambridge University Press

The models presented in (Kambe *et al.* 1985; Chang & Chen 1994) assume that the vortex is sufficiently far from the edge so that its trajectory is not altered in the vicinity of the edge. In that case the corresponding non-dimensional time unit scales as

$$T = \frac{U\tau}{L}, \tag{3.19}$$

where L the smallest distance to the edge (Kambe *et al.* 1985; Chang & Chen 1994). It is noted that l and L are in general different parameters since the first corresponds to the problem of vortices self-induced by the edge, while the second to the minimum distance for which a purely convected vortex passes near the edge without altering its trajectory. The non-dimensional frequency for the problem of pure-convection is $\tilde{\omega} = L/U\omega$ and hence the wavelengths can be expressed as

$$\lambda_U = \frac{2\pi L}{M}\frac{1}{\tilde{\omega}}, \tag{3.20}$$

where M is the Mach number. It can be seen that in that case the sound-wavelength depends on different parameters to those of the self-induction problem: convection velocity U and a distance $L \gg l$ where the vortex is located far enough from the edge that its trajectory is not affected by the image-vortex.

In real flows, for instance, in the vicinity of a trailing edge, turbulent eddies of different length scales interact with the edge resulting in acoustic radiation over a wide range of frequencies (Wang 2000; Colonius & Lele 2004). The distinction between purely edge-induction and convection effects is not clear. In the next section we therefore consider the combination of convection, and edge-effects on the trajectory of a point vortex in the vicinity of a corner and its influence on the sound field in order to provide a single model that contains the effects of convection (Kambe *et al.* 1985; Chang & Chen 1994) and self-induction around the edge (Crighton & Leppington 1971; Howe 1975*a*, 2003).

4. Convection and self-induction effects on vortex kinematics and sound

Turbulent fluctuations in the vicinity of an edge are influenced both by convection effects associated with the mean flow (here uniform velocity), and by near-edge vorticity. In the simplest case of a vortex-ring passing near the edge of a semi-infinite half-plane, experimental results have shown that its trajectory is influenced by its circulation as discussed in the works of Kambe *et al.* (1985) and in the appendix of Chen *et al.* (2022). We thus generalise the previous developments to account for a combination of these effects, both of which may influence the vortex path, hence the sound generation.

Consider a point vortex in a free stream, with velocity U, angle η with respect to the horizontal axis and which passes in the vicinity of a semi-infinite wedge. We cannot now choose, *a priori*, the closest distance to the edge as in (3.6). We therefore introduce the length scale l_0, which is the initial distance between the vortex and the edge (figure 6). The initial angle is θ_0. Equation (3.3) is used as in § 3 to obtain the kinematics of the point vortex. Convection of the vortex core is accounted for by adding the free stream complex velocity potential to (3.4):

$$F(z_0) = \frac{i\Gamma}{2\pi}\ln\left(\zeta(z) - \zeta^*(z_0)\right) + Uz_0e^{-i\eta}. \tag{4.1}$$

This results in a flow model with two velocity scales: one associated with the free stream flow U and another that can be considered as a generic, vortical fluctuation, such that $v \sim \Gamma/l_0$, where v is a characteristic vortical velocity associated with the circulation Γ.

https://doi.org/10.1017/jfm.2025.10580 Published online by Cambridge University Press

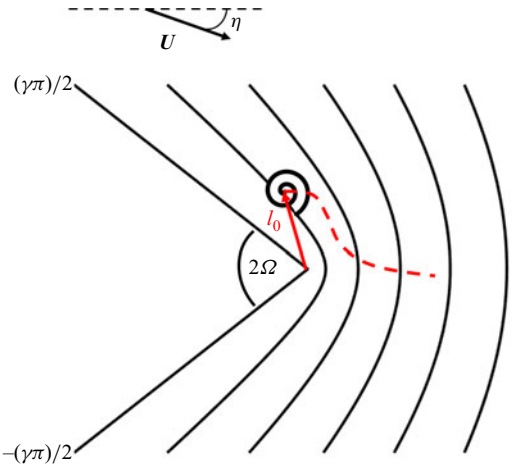


Figure 6. Motion of a vortex close to the edge by taking into account convection effects. The red-dashed line corresponds to the vortex trajectory and l_0 is a measure of its initial distance from the edge. The black solid lines correspond to the stream function related to the hypothetical velocity potential, as shown in § 3.1.

By performing the same calculations as in § 3.1 and Appendix A we obtain

$$\begin{pmatrix} \cos\theta_0 & -r_0\sin\theta_0 \\ \sin\theta_0 & r_0\cos\theta_0 \end{pmatrix} \frac{\mathrm{d}}{\mathrm{d}\tau}\begin{pmatrix} r_0 \\ \theta_0 \end{pmatrix} = \begin{pmatrix} \dfrac{\Gamma(\gamma-1)}{4\pi\gamma r_0}\sin\theta_0 + \dfrac{\Gamma}{4\pi\gamma r_0}\dfrac{\sin\left(\theta_0\frac{\gamma-1}{\gamma}\right)}{\cos(\theta_0/\gamma)} + U\cos\eta \\ \dfrac{-\Gamma(\gamma-1)}{4\pi\gamma r_0}\cos\theta_0 - \dfrac{\Gamma}{4\pi\gamma r_0}\dfrac{\cos\left(\theta_0\frac{\gamma-1}{\gamma}\right)}{\cos(\theta_0/\gamma)} + U\sin\eta \end{pmatrix}. \tag{4.2}$$

The system of (4.2) is solved with the method of determinants and the trajectory of the vortex is described by the coupled system of differential equations,

$$\begin{aligned} \dot{r}_0 &= -\frac{\Gamma}{4\pi\gamma r_0}\tan(\theta_0/\gamma) + U\cos(\theta_0-\eta), \\ \dot{\theta}_0 &= -\frac{\Gamma}{4\pi r_0^2} - \frac{U}{r_0}\sin(\theta_0-\eta), \end{aligned} \tag{4.3}$$

where the upper dot denotes the first time derivative. The system of (4.3) cannot be solved analytically, however, it is possible to gain insight regarding the key parameters of the problem. By introducing the non-dimensional quantities $\bar{r_0} = r_0/l_0$, $\dot{\bar{r}}_0 = \dot{r}_0/U$ and $\dot{\bar{\theta}}_0 = \dot{\theta}_0 l_0/U$, we obtain

$$\begin{aligned} \dot{\bar{r}}_0 &= -\frac{\Lambda}{\gamma\bar{r}_0}\tan(\theta_0/\gamma) + \cos(\theta_0-\eta), \\ \dot{\bar{\theta}}_0 &= -\frac{\Lambda}{\bar{r_0}^2} - \frac{\sin(\theta_0-\eta)}{\bar{r}_0}, \end{aligned} \tag{4.4}$$

where Λ is a non-dimensional parameter, that we refer to as the wedge-deflection effect:

$$\Lambda \equiv \Gamma/(4\pi U l_0) = v/(4\pi U). \tag{4.5}$$

In regions with strong circulation or very close to the edge, the velocity field induced by the vortex is dominant and Λ takes large values. On the other hand, far from the edge

https://doi.org/10.1017/jfm.2025.10580 Published online by Cambridge University Press

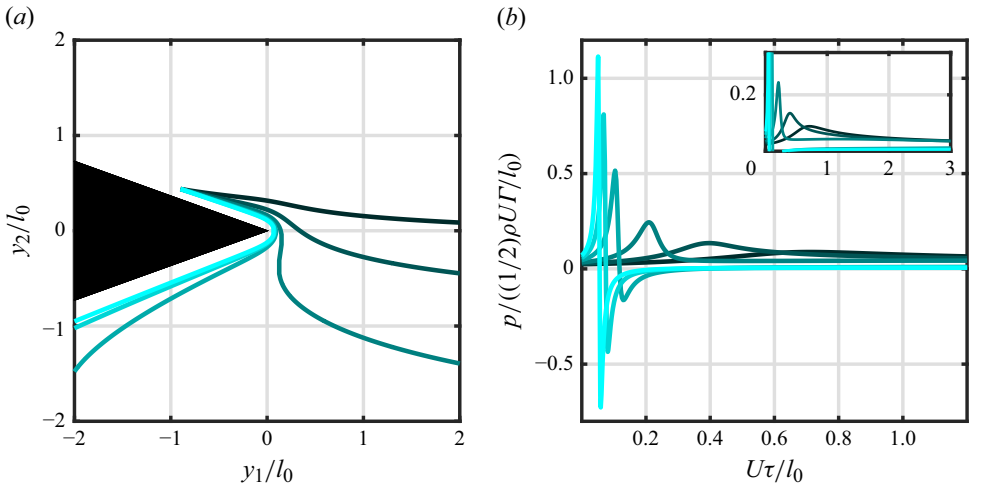


Figure 7. Influence of parameter Λ on vortex trajectories (a) and far-field pressure signature (b). Different vortex paths are shown in (a) and the corresponding pressure signatures in (b). The darker colours correspond to lower values of Λ, while the lighter colours to higher values. The results are shown for $l_0 = 0.2$ m, $\theta_0 = \gamma\pi/2 - \pi/20$, $U = 30\,\mathrm{m\,s^{-1}}$, $\Omega = 20°$, an observer in the far field $r = 5l_0$ and $\Lambda = \{0.1; 0.25; 0.5; 1; 1.5; 2\}$ and $\eta = 0$.

or in regions where vorticity is weak, convection effects dominate and Λ decreases. For instance, in the extreme case of $\Lambda \gg 1$ (strong circulation and/or close to the edge and/or very low speed flow) (4.4) results asymptotically in the equations of motion obtained in the previous subsection. In the other extreme case of $\Lambda \ll 1$ (weak circulation and/or far from the edge and/or higher Mach number flow), it yields the equations of motion of a vortex convected by the mean flow, for a constant free stream velocity U the vortex follows a straight line as in the model of Kambe *et al.* (1985).

A similar analysis restricted to the case of the half-plane was presented by Hardin (1980) in an attempt to model the noise generated by vortices formed at the side edges of flaps. In Hardin's work it is assumed that the vortex is either carried by the potential flow in the vicinity of the edge or its trajectory is deflected by the influence of the edge. In his analysis the term $Uz_0e^{-i\eta}$ in (4.1) is replaced by $U\sqrt{z_0}$ to account for the local potential flow around the half-plane. In the absence of the edge-effects on the vortex path the latter would yield a silent vortex since its path would match with the streamlines of the potential flow around the wedge (as given by (3.1)). However, in the present study we are interested in the convection of the vortex by the free stream velocity.

The system of (4.3) is solved numerically by implementing a Runge–Kutta scheme of fourth order, and (3.2) is used to compute the pressure field. Figure 7 shows a comparison of the far-field pressure pulse generated by vortices subjected to a varying degree of wedge-effect strengths. At a first step, we consider $\eta \approx 0$ to focus on the influence of the wedge-deflection effect on the kinematics of the vortex and the acoustic field. It is observed that for large values of Λ the problem reduces to that of § 3.1. Furthermore, a change of sign in the pressure pulse is observed when the vortex passes the bisector of the wedge. As the wedge-deflection effect decreases, the negative peak of the far-field pressure pulse tends to vanish since the vortex is convected downstream and does not move towards the other face of the wedge, $\theta_0 \in (0, -\gamma\pi/2]$. This can be explained by the fact that the basic mechanism of sound generation is the crossing of the vortex path with the hypothetical streamlines around the wedge. When convection effects are absent the vortex path is symmetric around

https://doi.org/10.1017/jfm.2025.10580 Published online by Cambridge University Press

the edge and it becomes parallel to the streamlines of the hypothetical potential flow at $\theta_0 = 0$. Then it passes to the lower side of the wedge, where $\theta_0 < 0$. When convection effects become important, the vortex trajectory changes such that it does not become parallel to the hypothetical streamlines and thus there is no change of sign. The results can be further investigated by rewriting the far-field pressure signature in the following form:

$$p\,(r, \theta, \tau) = -\rho \sin\left(\frac{\theta}{\gamma}\right) r^{\frac{1}{\gamma}} \frac{\Gamma U}{l_0^{(1-1/\gamma)}} f\,(\Lambda, \gamma, \bar{r}_0, \theta_0, \eta), \tag{4.6}$$

where $f(\Lambda, \gamma, \bar{r}_0, \theta_0, \eta)$ corresponds to a function that depends on the vortex trajectory,

$$f\,(\Lambda, \gamma, \bar{r}_0, \theta_0, \eta) = \bar{r}_0^{\frac{1}{\gamma}} \left[\frac{\Lambda}{\bar{r}_0^2} \sin\left(\theta_0/\gamma\right) \left(\frac{1-\gamma}{\gamma}\right) - \frac{\cos\left(\eta - \theta_0 \frac{\gamma-1}{\gamma}\right)}{\bar{r}_0} \right]. \tag{4.7}$$

The influence of the main parameters of the problem is clearer in (4.6) and (4.7). The amplitude depends mainly on the flow velocity, the circulation and the distance from the edge as is indicated by the factor $\Gamma U / l_0^{(1-1/\gamma)}$. Further conclusions can be drawn by examining (4.7). The function f can be decomposed into two terms, one that corresponds to the influence of the vortex close to the edge and a convection term. We therefore have

$$f = f_1\,(\Lambda, \bar{r}_0, \theta_0, \gamma) + f_2\,(\eta, \bar{r}_0, \theta_0, \gamma). \tag{4.8}$$

When $\bar{r_0}$ is small, the sound pressure field is mainly influenced by $f_1(\Lambda, \bar{r}_0, \theta_0, \gamma)$. On the contrary as the vortex is convected away from the edge, f_1 decreases as $\bar{r}_0^{1/\gamma-2}$ and convection effects take over ($\bar{r}_0^{1/\gamma-1}$).

As the wedge angle increases the vortex structures (here point vortices) move parallel to the face of the wedge before shed in the wake. Therefore, we now consider an incidence angle equal to the half-wedge angle Ω and investigate the effect of the wedge angle on the vortex path and the acoustic field. The results are shown in figure 8 for a constant value of the wedge-deflection parameter ($\Lambda = 0.25$) and different wedge angles and angles of incidence $\eta = -\Omega$. It should be noted that in the absence of convection effects, the increase of the wedge angle results in slightly higher frequency radiation (§ 3.2). However, when both convection and edge-induction effects on the vortex path are present, vortices near sharp wedges tend to be more strongly influenced by the edge, while as the wedge angle increases the relative effect of edge induction is reduced, resulting in longer pulses with lower amplitudes. This illustrates the importance of considering both convection and edge-induction effects in modelling the aeroacoustics of sources in the vicinity of an edge.

The directivity of the acoustic field depends solely on the parameter $\sin(\theta/\gamma)$ for both models developed. Directivity plots for different wedge half-angles are depicted in figure 9 which shows the typical cardioid shape, characteristic of low-frequency diffraction by semi-infinite half-planes and rigid corners (Howe 2001; Roger *et al.* 2016). Note that the directivity is shown at the non-dimensional time when the vortex reaches its minimum radial distance from the edge.

The previous theoretical investigation highlighted that the interplay between convection and self-induction due to near-edge vorticity affects the kinematics of a point vortex interacting with a rigid corner and the corresponding sound-field. In actual flows, the idealised point-vortex hypothesis is not valid, however, the proposed analysis allows a qualitative description of several aeroacoustic problems. Particularly, the wedge deflection parameter allows us to extend the modelling approaches by relaxing the frozen gust assumption for a point vortex (turbulent fluctuation in the vicinity of the edge). The latter

https://doi.org/10.1017/jfm.2025.10580 Published online by Cambridge University Press

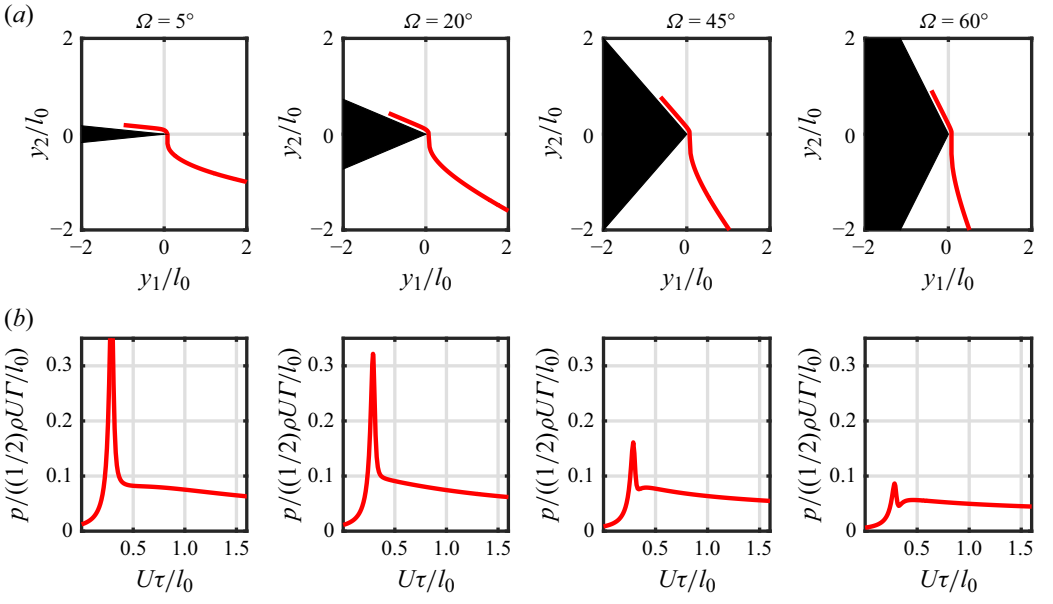


Figure 8. Vortex path (*a*) and normalised time-domain acoustic pressure signature (*b*) for different wedge angles ($\Omega = 5°, 20°, 45°, 60°$), constant wedge-deflection parameter $\Lambda = 0.25$, angle of incidence $\eta = -\Omega$ and an observer located at $(r, \theta) = (20l_0, \gamma\pi/2)$.

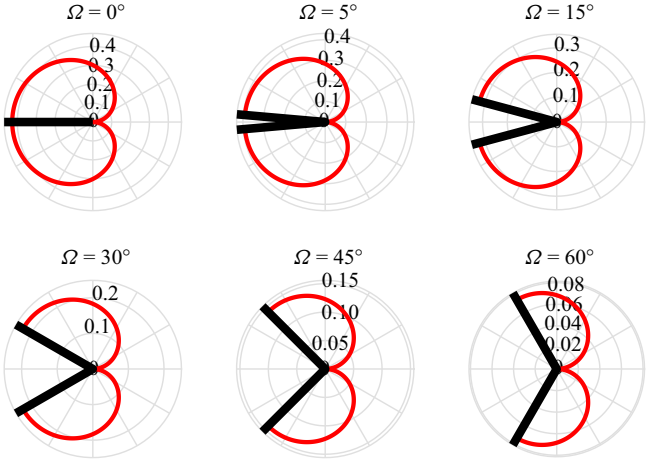


Figure 9. Directivity plots obtained for different wedge angles. The acoustic-field is shown for $\Lambda = 0.25$, $\eta = -\Omega$ and $r = 20l_0$, at the time instant when the vortex reaches its minimum radial distance from the edge. Note that for each sub-plot the radius axis of the polar plots, corresponding to the amplitude of the acoustic pressure, is adjusted accordingly to enhance the visualisation of directivity pattern. The results are consistent with decreasing amplitude as Ω increases.

has been proven successful in the classical trailing-edge noise modelling (Amiet 1975; Howe 1978), while it fails to produce accurate results when applied to serrated trailing-edges (Moreau & Doolan 2013; Avallone *et al.* 2018; Tiomkin & Jaworski 2024), where the hydrodynamic field is strongly affected by the presence of the edge. In the limiting case of small values of Λ the proposed analysis is in agreement with the frozen gust assumption, since the point vortex passes near the edge without altering its trajectory. On the contrary,

https://doi.org/10.1017/jfm.2025.10580 Published online by Cambridge University Press

as Λ increases, the more we deviate from this hypothesis. Provided that the noise generated by a serrated trailing edge consists of a more complex three-dimensional (3-D) flow field, the proposed model could be adapted to explore the sound field produced due to the streamwise vorticity on the serration (see figure 6 of Avallone, Pröbsting & Ragni 2016) and also provide a simplified description for the interaction between the main vortices and the trailing edge by appropriately informing the wedge-deflection parameter. A more detailed classification and comparison of the vortex structures near serrated trailing edges is, however, out of the scope of the present work.

5. Conclusions and discussion on extensions to applied problems

We have considered the kinematics and aeroacoustics of point vortices in the vicinity of a wedge-shaped edge. In a first step, the point vortices are considered close to the edge (solely influenced by the image vortex), neglecting convection effects. Closed-form solutions are obtained for the radiated sound in both time and frequency domains, and these show how the scattered sound depends only on the wedge angle, circulation and the shortest distance from the edge. An extension of the model accounts for convection effects and shows that there exists a non-dimensional wedge-deflection parameter that dominates the kinematics of the vortex close to the edge. Large values of the wedge-deflection parameter correspond to vortex trajectories dominated by self-induction around the edge that radiate at high frequencies, while low values of the parameter indicate trajectories dominated by convection, leading to lower-frequency radiation. Finally, it was shown that for a constant value of the wedge-deflection, as the wedge angle increases the convection effect becomes dominant, leading to lower-frequency radiation with lower amplitude.

To conclude, the proposed model incorporates features from various independent studies found in the literature such as diffraction by semi-infinite wedges (Crighton & Leppington 1970; Chang & Chen 1994) and the sensitivity of the vortex path on edge-induction (Crighton 1972; Howe 1975*a*) and convection effects (Kambe *et al.* 1985; Chang & Chen 1994) to examine the sound-field of vortex–wedge interactions. The foregoing analysis thus provides a more general and complete physical insight in the competing flow mechanisms (edge-induction and convection) that drive the motion of the vortex near an edge of arbitrary angle and dominate the sound field. Table 1 summarises the existing models and shows the contributions of the one proposed in this study.

In addition to the theoretical contributions in edge-vortex interaction noise, the proposed model could further assist in identifying sound-generation mechanisms of more complex flows. A detailed analysis is out of the scope of the present paper and could be provided in a subsequent study; however, we give an example of its potential use. Recent approaches aiming to explore bluff-body noise (Prinja, Jordan & Margnat 2025) and more specifically airfoil noise (Sano *et al.* 2019; Demange *et al.* 2024*a*,*b*; Yuan *et al.* 2024) adapted the strategy of describing the aeroacoustic source in terms of coherent flow structures (motions), which has been successfully applied in jet-noise modelling (Jordan & Colonius 2013). The extraction of those coherent structures is achieved either by postprocessing techniques on experimental or simulation data (Sano *et al.* 2019) or by physics-based models such as resolvent analysis (Demange *et al.* 2024*b*). Both approaches decompose the flow field in modes that contribute to the total flow or acoustic energy. These acoustically important structures can be used to inform the present model and provide an in-depth exploration of the sound generation mechanism due to edge vortex interactions, expressed in terms of a non-dimensional parameter. Similar approaches could be adapted to investigate the aeroacoustics of vorticity-edge interactions for larger wedge angles

https://doi.org/10.1017/jfm.2025.10580 Published online by Cambridge University Press

Model	Geometry	Assumptions	Contribution
(Crighton 1972)	Half-plane	2-D, no convection.	Analytical expressions using singular perturbation method.
(Howe 2003)	Half-plane	2-D compact green function; no convection.	Vortex-sound model; analytical expressions; enhanced physical interpretation.
(Kambe *et al.* 1985)	Half-plane	No edge effects on vortex path.	3-D; studies convection effects.
(Chang & Chen 1994)	Wedge	Same as (Kambe *et al.* 1985).	Extends to wedge geometry.
(Chen *et al.* 2022)	Half-plane	Same as (Kambe *et al.* 1985).	Porous edge extension of (Kambe *et al.* 1985).
Present (§ 3)	Wedge	2-D compact green function; no convection.	Extends (Howe 2003) to wedge geometry.
Present (§ 4)	Wedge	2-D compact Green function.	Convection & edge effects; wedge deflection parameter.

Table 1. Comparison of vortex–edge interaction models. All approaches assume long wavelengths relative to vortex–edge distance ($kl \ll 1$).

($\Omega \approx 45°$), such as the noise generated by side-view mirrors (Stoffel *et al.* 2025), or side edges of flaps (Roger *et al.* 2016).

Supplementary material. Supplementary material are available at https://doi.org/10.1017/jfm.2025.10580.

Funding. This work was supported by the DGAC (Direction Générale de l'Aviation Civile), by the PNRR (Plan National de Relance et de Résilience Français) and by NextGeneration EU via the project MAMBO (Méthodes Avancées pour la Modélisation du Bruit moteur et aviOn).

Declaration of interests. The authors report no conflict of interest.

Appendix A. Derivation steps of (3.6), (3.7)

In this appendix the derivation of the vortex path and the far field pressure signature of (3.6), (3.7) are presented. The velocity, obtained by the complex velocity potential is written as

$$\frac{\mathrm{d}z_0^*}{\mathrm{d}\tau} = -i\frac{\Gamma\zeta''(z_0)}{4\pi\zeta'(z_0)} + \frac{\mathrm{d}}{\mathrm{d}z_0}\left[\frac{i\Gamma}{2\pi}\ln\left(\zeta(z) - \zeta^*(z_0)\right)\right]. \tag{A1}$$

Substituting

$$\zeta(z_0) = iz_0^{1/\gamma} = ir_0^{1/\gamma}e^{i\theta_0/\gamma} \tag{A2}$$

it yields

$$\frac{\mathrm{d}}{\mathrm{d}\tau}\{r_0\cos\theta_0 - ir_0\sin\theta_0\} = \frac{\Gamma}{4\pi\gamma r_0}\left[(\gamma-1)\sin\theta + \frac{\sin\left(\theta_0\dfrac{\gamma-1}{\gamma}\right)}{\cos\left(\dfrac{\theta_0}{\gamma}\right)}\right] + \frac{i\Gamma}{4\pi\gamma r_0}\left[(\gamma-1)\cos\theta + \frac{\cos\left(\theta_0\dfrac{\gamma-1}{\gamma}\right)}{\cos\left(\dfrac{\theta_0}{\gamma}\right)}\right]. \tag{A3}$$

https://doi.org/10.1017/jfm.2025.10580 Published online by Cambridge University Press

By taking the derivative in time and separating the real and imaginary parts of the complex number, the following system of equations is obtained:

$$\begin{pmatrix} \cos\theta_0 & -r_0\sin\theta_0 \\ \sin\theta_0 & r_0\cos\theta_0 \end{pmatrix} \frac{\mathrm{d}}{\mathrm{d}\tau}\begin{pmatrix} r_0 \\ \theta_0 \end{pmatrix} = \begin{pmatrix} \dfrac{\Gamma(\gamma-1)}{4\pi\gamma r_0}\sin\theta_0 + \dfrac{\Gamma}{4\pi\gamma r_0}\dfrac{\sin\left(\theta_0\frac{\gamma-1}{\gamma}\right)}{\cos\left(\theta_0/\gamma\right)} \\ \dfrac{-\Gamma(\gamma-1)}{4\pi\gamma r_0}\cos\theta_0 - \dfrac{\Gamma}{4\pi\gamma r_0}\dfrac{\cos\left(\theta_0\frac{\gamma-1}{\gamma}\right)}{\cos\left(\theta_0/\gamma\right)} \end{pmatrix}. \tag{A4}$$

The solution of (A4) is obtained by the method of determinants and the following trigonometric relations are used:

$$\cos x\sin y - \sin x\cos y = -\sin(x-y), \tag{A5}$$
$$\cos x\cos y + \sin x\sin y = -\cos(x-y). \tag{A6}$$

It follows that

$$\frac{\mathrm{d}r_0}{\mathrm{d}\tau} = -\frac{\Gamma}{4\pi\gamma r_0}\tan(\theta/\gamma), \tag{A7}$$
$$\frac{\mathrm{d}\theta_0}{\mathrm{d}\tau} = -\frac{\Gamma}{4\pi r_0^2}. \tag{A8}$$

From (A8), (A7) it follows that

$$r_0\frac{\mathrm{d}\theta_0}{\mathrm{d}r_0} = \gamma\cot\left(\frac{\theta_0}{\gamma}\right) \tag{A9}$$

that leads to

$$\int_{\theta_{0,i}}^{\theta_0}\gamma^{-1}\tan\left(\xi/\gamma\right)\mathrm{d}\xi = \int_{r_{0,i}}^{r_0}x^{-1}\mathrm{d}x \Rightarrow r_0 = l\sec\left(\theta_0/\gamma\right), \tag{A10}$$

where $r_{0,i}$, $\theta_{0,i}$ the initial radial and angular coordinates of the vortex and l is the smallest distance between the vortex and the edge, defined as $l = r_{0,i}\cos(\theta_{0,i})$. Then, substituting (A10) into (A8) and following Howe's notation it yields

$$\begin{aligned} r_0(\tau) &= l\sqrt{1+(2\tilde{\tau}/\gamma)^2}, \\ \theta_0(\tau) &= \gamma\tan^{-1}(-2\tilde{\tau}/\gamma), \end{aligned} \tag{A11}$$

where $\tilde{\tau} = (\tau\Gamma)/(8\pi l^2)$. Furthermore, by combining (A11) and (3.2) and using the identities

$$\cos\left[\tan^{-1}x\right] = \left(x^2+1\right)^{-1/2}, \tag{A12}$$
$$\sin\left[\tan^{-1}(-x)\right] = -\frac{x}{\sqrt{x^2+1}}, \tag{A13}$$

results in (3.7).

https://doi.org/10.1017/jfm.2025.10580 Published online by Cambridge University Press

Appendix B. Frequency domain representation

Starting from (3.7), the acoustic pulse generated by a vortex which is self-induced close to a semi-infinite rigid wedge is given by

$$\begin{aligned} p(r,\theta,\tilde{\tau},\Gamma,l,\gamma) &= C(\theta/\gamma,\Gamma,l)T_{wedge}(r,l,\tilde{\tau},\gamma),\\ C(\theta/\gamma,\Gamma,l) &= \frac{\rho\Gamma^2}{8\pi^2 l^2}\sin(\theta/\gamma),\\ T_{wedge}(r,l,\tilde{\tau},\gamma) &= 2\frac{(rl)^{1/\gamma}}{r}\left(\frac{\gamma-1}{\gamma^2}\right)\left[\frac{2\tilde{\tau}/\gamma}{\left[1+(2\tilde{\tau}/\gamma)^2\right]^{\frac{3\gamma-1}{2\gamma}}}\right]. \end{aligned} \tag{B1}$$

Its frequency domain counterpart is obtained as follows. We write the Fourier-transformed quantity as

$$\begin{aligned} \hat{p}(r,\theta,\tilde{\omega},\Gamma,l,\gamma) &= C(\theta/\gamma,\Gamma,l)\hat{T}_{wedge}(r,l,\tilde{\omega},\gamma),\\ C(\theta/\gamma,\Gamma,l) &= \frac{\rho\Gamma^2}{8\pi^2 l^2}\sin(\theta/\gamma),\\ \hat{T}_{wedge}(r,l,\tilde{\tau},\gamma) &= 2\frac{(rl)^{1/\gamma}}{r}\left(\frac{\gamma-1}{\gamma^2}\right)\int_{-\infty}^{\infty}\frac{2\tilde{\tau}/\gamma}{\left[1+(2\tilde{\tau}/\gamma)^2\right]^{\frac{3\gamma-1}{2\gamma}}}e^{-i\omega\tau}\mathrm{d}\tau, \end{aligned} \tag{B2}$$

where $\tilde{\omega}$ is the non-dimensional frequency, that will be obtained in the following calculations by changing the integration variable. The dependence on the frequency and the wedge angle is captured by $\hat{T}_{wedge}$, while C shows a dependence on the amplitude and the directivity. Furthermore, we write $\hat{T}_{wedge}$ as

$$\begin{aligned} \hat{T}_{wedge}(r,l,\tilde{\omega},\gamma) &= 2\frac{(rl)^{1/\gamma}}{r}\left(\frac{\gamma-1}{\gamma^2}\right)\\ &\quad\times\int_{-\infty}^{\infty}2\tilde{\tau}/\gamma\left[1+(2\tilde{\tau}/\gamma)^2\right]^{\frac{1-3\gamma}{2\gamma}}e^{-i\omega\tau}\mathrm{d}\tau. \end{aligned} \tag{B3}$$

Then we factorise the terms in the brackets as

$$\begin{aligned} \left[1+(2\tilde{\tau}/\gamma)^2\right]^{\frac{1-3\gamma}{2\gamma}} &= \left[4/\gamma^2\left(\gamma^2/4+\tilde{\tau}^2\right)\right]^{\frac{1-3\gamma}{2\gamma}}\\ &= \left(\frac{4}{\gamma^2}\right)^{\frac{1}{2\gamma}-3/2}\left[\left(\gamma^2/4+\tilde{\tau}^2\right)\right]^{\frac{1}{2\gamma}-3/2}. \end{aligned} \tag{B4}$$

As a result, (B3) becomes

$$\begin{aligned} \hat{T}_{wedge}(r,l,\tilde{\omega},\gamma) &= \frac{(rl)^{1/\gamma}}{r}\frac{4}{\gamma}\left(\frac{\gamma-1}{\gamma^2}\right)\left(\frac{4}{\gamma^2}\right)^{\frac{1}{2\gamma}-3/2}\\ &\quad\times\int_{-\infty}^{\infty}\tilde{\tau}\left[\frac{\gamma^2}{4}+\tilde{\tau}^2\right]^{\frac{1}{2\gamma}-3/2}e^{-i\omega\tau}\mathrm{d}\tau. \end{aligned} \tag{B5}$$

Since we are working with the non-dimensional units $\tilde{\tau}$, we make the following change of variable:

$$\tilde{\tau}=\frac{\Gamma}{8\pi l^2}\tau\Rightarrow\tau=\frac{8\pi l^2}{\Gamma}\tilde{\tau},\ \mathrm{d}\tau=\frac{8\pi l^2}{\Gamma}\mathrm{d}\tilde{\tau}, \tag{B6}$$

https://doi.org/10.1017/jfm.2025.10580 Published online by Cambridge University Press

and combining (B5), (B6) we obtain

$$\hat{T}_{wedge}\left(r, l, \tilde{\omega}, \gamma\right) = \frac{8\pi l^2}{\Gamma}\frac{(rl)^{1/\gamma}}{r}\frac{4}{\gamma}\left(\frac{\gamma-1}{\gamma^2}\right)\left(\frac{4}{\gamma^2}\right)^{\frac{1}{2\gamma}-3/2} \times \int_{-\infty}^{\infty}\tilde{\tau}\left[\frac{\gamma^2}{4}+\tilde{\tau}^2\right]^{\frac{1}{2\gamma}-3/2} e^{-i\tilde{\omega}\tilde{\tau}}\mathrm{d}\tilde{\tau}, \tag{B7}$$

where

$$\tilde{\omega} = \frac{8\pi l^2}{\Gamma}\omega, \tag{B8}$$

which corresponds to wavelengths

$$\frac{\lambda}{l} = \frac{1}{\tilde{\omega}}\frac{16\pi^2 l c_0}{\Gamma}. \tag{B9}$$

Moreover, we write the exponential as

$$e^{-i\tilde{\omega}\tilde{\tau}} = \cos\left(\tilde{\omega}\tilde{\tau}\right) - i\,\sin\left(\tilde{\omega}\tilde{\tau}\right), \tag{B10}$$

and the integrals of (B7) becomes

$$\int_{-\infty}^{\infty}\tilde{\tau}\left[\frac{\gamma^2}{4}+\tilde{\tau}^2\right]^{\frac{1}{2\gamma}-3/2} e^{-i\tilde{\omega}\tilde{\tau}}\mathrm{d}\tilde{\tau} = \int_{-\infty}^{\infty}F\left(\tilde{\tau}\right)d\tilde{\tau} - i\int_{-\infty}^{\infty}G(\tilde{\tau})\mathrm{d}\tilde{\tau}, \tag{B11}$$

where

$$\begin{aligned} F(\tilde{\tau}) &= \tilde{\tau}\left[\frac{\gamma^2}{4}+\tilde{\tau}^2\right]^{\frac{1}{2\gamma}-3/2}\cos\left(\tilde{\omega}\tilde{\tau}\right), \quad \text{where } F\left(-\tilde{\tau}\right) = -F\left(\tilde{\tau}\right), \\ G\left(\tilde{\tau}\right) &= \tilde{\tau}\left[\frac{\gamma^2}{4}+\tilde{\tau}^2\right]^{\frac{1}{2\gamma}-3/2}\sin\left(\tilde{\omega}\tilde{\tau}\right), \quad \text{where } G\left(-\tilde{\tau}\right) = G(\tilde{\tau}). \end{aligned} \tag{B12}$$

Since $F(\cdot)$ is an odd function, the integration over $\tilde{\tau}\in(-\infty,\infty)$ yields zero, and then only the second integral of the right-hand side of (B11) needs to be calculated. Since G is an even function we may write

$$\int_{-\infty}^{\infty}\tilde{\tau}\left[\frac{\gamma^2}{4}+\tilde{\tau}^2\right]^{\frac{1}{2\gamma}-3/2} e^{-i\tilde{\omega}\tilde{\tau}}\mathrm{d}\tilde{\tau} = -2i\int_{0}^{\infty}G(\tilde{\tau})\mathrm{d}\tilde{\tau}. \tag{B13}$$

The integral of (B13) is computed analytically for $\gamma\in[2,\,1]$ by using the formula (2.10), p.121 in Oberhettinger (2012):

$$\int_0^{\infty} x\left(a^2+x^2\right)^{\nu-3/2}\sin(yx)\mathrm{d}x = \frac{\sqrt{\pi}\,(2a)^{\nu}}{2\tilde{\Gamma}\left(\frac{3}{2}-\nu\right)}y^{1-\nu}K_{\nu}\left(ay\right),\ Re[\nu]<1, \tag{B14}$$

where $\tilde{\Gamma}(\cdot)$ is the gamma function and

$$K_{\nu}(z) = \frac{i\pi}{2}e^{i\frac{\pi}{2}\nu}H_{\nu}^{(1)}\left(ze^{i\pi/2}\right) \tag{B15}$$

https://doi.org/10.1017/jfm.2025.10580 Published online by Cambridge University Press

is the modified Bessel function and $H_v^{(1)}$ the Hankel function of the first kind. It follows that

$$\begin{aligned}\int_{-\infty}^{\infty} \tilde{\tau}\left[\frac{\gamma^2}{4}+\tilde{\tau}^2\right]^{\frac{1}{2\gamma}-3/2} e^{-i\tilde{\omega}\tilde{\tau}}\mathrm{d}\tilde{\tau} &= -2i\int_0^{\infty} G\left(\tilde{\tau}\right)\mathrm{d}\tilde{\tau}\\ &= -2i\frac{\sqrt{\pi}\left(\frac{\gamma^2}{2}\right)^{\frac{1}{2\gamma}}}{2\tilde{\Gamma}\left(\frac{3}{2}-\frac{1}{2\gamma}\right)}\tilde{\omega}^{1-\frac{1}{2\gamma}}K_{\frac{1}{2\gamma}}\left(\frac{\gamma^2}{4}\tilde{\omega}\right).\end{aligned} \tag{B16}$$

From (B7), (B16) it follows that

$$\begin{aligned}\hat{T}_{wedge}\left(r,l,\tilde{\tau},\gamma\right) = &-i\frac{8\pi l^2}{\Gamma}\frac{(rl)^{1/\gamma}}{r}\frac{4}{\gamma}\left(\frac{\gamma-1}{\gamma^2}\right)\left(\frac{4}{\gamma^2}\right)^{\frac{1}{2\gamma}-3/2}\\ &\times\frac{\sqrt{\pi}\left(\frac{\gamma^2}{2}\right)^{\frac{1}{2\gamma}}}{\tilde{\Gamma}\left(\frac{3}{2}-\frac{1}{2\gamma}\right)}\tilde{\omega}^{1-\frac{1}{2\gamma}}K_{\frac{1}{2\gamma}}\left(\frac{\gamma^2}{4}\tilde{\omega}\right).\end{aligned} \tag{B17}$$

Finally the Fourier-transformed expression is given as

$$\begin{aligned}\hat{p}\left(r,\theta,\tilde{\omega},\Gamma,l,\gamma\right) &= \tilde{C}\left(\theta/\gamma\right)\hat{T}_{wedge}\left(r,l,\tilde{\omega},\gamma\right),\\ \tilde{C}\left(\theta/\gamma\right) &= \rho\sin\left(\theta/\gamma\right),\\ \hat{T}_{wedge}\left(r,l,\tilde{\omega},\gamma\right) = &-i\frac{(rl)^{1/\gamma}}{r}\frac{4}{\gamma}\left(\frac{\gamma-1}{\gamma^2}\right)\left(\frac{4}{\gamma^2}\right)^{\frac{1}{2\gamma}-3/2}\\ &\times\frac{\sqrt{\pi}\left(\frac{\gamma^2}{2}\right)^{\frac{1}{2\gamma}}}{\tilde{\Gamma}\left(\frac{3}{2}-\frac{1}{2\gamma}\right)}\tilde{\omega}^{1-\frac{1}{2\gamma}}K_{\frac{1}{2\gamma}}\left(\frac{\gamma^2}{4}\tilde{\omega}\right).\end{aligned} \tag{B18}$$

References

Abreu, L.I., Tanarro, A., Cavalieri, A.V.G., Schlatter, P., Vinuesa, R., Hanifi, A. & Henningson, D.S. 2021 Spanwise-coherent hydrodynamic waves around flat plates and airfoils. *J. Fluid Mech.* **927**, A1.

Amiet, R.K. 1975 Acoustic radiation from an airfoil in a turbulent stream. *J. Sound Vib.* **41** (4), 407–420.

Avallone, F., Pröbsting, S. & Ragni, D. 2016 Three-dimensional flow field over a trailing-edge serration and implications on broadband noise. *Phys. Fluids* **28** (11), 117101.

Avallone, F., van der Velden, W.C.P., Ragni, D. & Casalino, D. 2018 Noise reduction mechanisms of sawtooth and combed-sawtooth trailing-edge serrations. *J. Fluid Mech.* **848**, 560–591.

Biot, M.A. & Tolstoy, I. 1957 Formulation of wave propagation in infinite media by normal coordinates with an application to diffraction. *J. Acoust. Soc. Am.* **29** (3), 381–391.

Cavalieri, A.V.G., Jordan, P., Wolf, W.R. & Gervais, Y. 2014 Scattering of wavepackets by a flat plate in the vicinity of a turbulent jet. *J. Sound Vib.* **333** (24), 6516–6531.

Chang, C.-C. & Chen, T.-L. 1994 Acoustic emission by a vortex ring passing near a sharp wedge. *Proc. R. Soc. Lond. A: Math. Phys. Sci.* **445**, 141–155.

Chen, H., Yoas, Z.W., Jaworski, J.W. & Krane, M.H. 2022 Acoustic emission of a vortex ring near a porous edge. Part 1: theory. *J. Fluid Mech.* **941** , A28.

Colonius, T. & Lele, S.K. 2004 Computational aeroacoustics: progress on nonlinear problems of sound generation. *Prog. Aerosp. Sci.* **40** (6), 345–416.

https://doi.org/10.1017/jfm.2025.10580 Published online by Cambridge University Press

CRIGHTON, D.G. & LEPPINGTON, F.G. 1971 On the scattering of aerodynamic noise. *J. Fluid Mech.* **46** (3), 577–597.

CRIGHTON, D.G. 1972 Radiation from vortex filament motion near a half plane. *J. Fluid Mech.* **51** (2), 357–362.

CRIGHTON, D.G. & LEPPINGTON, F.G. 1970 Scattering of aerodynamic noise by a semi-infinite compliant plate. *J. Fluid Mech.* **43** (4), 721–736.

CURLE, N. 1955 The influence of solid boundaries upon aerodynamic sound.. *Proc. R. Soc. Lond. A: Math. Phys. Sci.* **231**, 505–514.

DEMANGE, S., YUAN, Z., CAVALIERI, A.V.G., HANIFI, A. & OBERLEITHNER, K. 2024*a* Wavepackets driving trailing edge noise. Part II–resolvent-based model. In 30th AIAA/CEAS Aeroacoustics Conference (2024), pp. 3170.

DEMANGE, S., YUAN, Z., JEKOSCH, S., HANIFI, A., CAVALIERI, A.V.G., SARRADJ, E., KAISER, T.L. & OBERLEITHNER, K. 2024*b* Resolvent model for aeroacoustics of trailing edge noise. *Theor. Comput. Fluid Dyn.* **38**, 163–183.

DOOLAN, C.J. & MOREAU, D.J. 2015 A review of airfoil trailing edge noise with some implications for wind turbines. *Intl J. Aeroacoust.* **14** (5-6), 811–832.

FFOWCS WILLIAMS, J.E. & HAWKINGS, D.L. 1969 Sound generation by turbulence and surfaces in arbitrary motion. *Phil. Trans. R. Soc. Lond. A: Math. Phys. Sci.* 321–342.

FFOWCS WILLIAMS, J.E. & HALL, L.H. 1970 Aerodynamic sound generation by turbulent flow in the vicinity of a scattering half plane. *J. Fluid Mech.* **40** (4), 657–670.

GUO, Y. 2011 Aircraft flap side edge noise modeling and prediction. In 17th AIAA/CEAS Aeroacoustics Conference (32nd AIAA Aeroacoustics Conference), pp. 2731.

HARDIN, J.C. 1980 Noise radiation from the side edges of flaps. *AIAA J.* **18** (5), 549–552.

HOWE, M.S. 1975*a* Contributions to the theory of aerodynamic sound, with application to excess jet noise and the theory of the flute. *J. Fluid Mech.* **71** (4), 625–673.

HOWE, M.S. 1975*b* The generation of sound by aerodynamic sources in an inhomogeneous steady flow. *J. Fluid Mech.* **67** (3), 597–610.

HOWE, M.S. 1998 *Acoustics of Fluid-Structure Interactions*. Cambridge University Press.

HOWE, M.S. 2001 Edge-source acoustic green's function for an airfoil of arbitrary chord, with application to trailing-edge noise. *Q. J. Mech. Appl. Maths* **54** (1), 139–155.

HOWE, M.S. 1978 A review of the theory of trailing edge noise. *J. Sound Vib.* **61** (3), 437–465.

HOWE, M.S. 2003 *Theory of Vortex Sound*. Cambridge University press.

HUBER, J., PONT, G., JORDAN, P. & ROGER, M. 2024 Wavepacket modelling of jet-flap interaction noise: from laboratory to full-scale aircraft. *Flow Turbul. Combust.* **113** (3), 773–802.

JORDAN, P. & COLONIUS, T. 2013 Wave packets and turbulent jet noise. *Annu. Rev. Fluid Mech.* **45** (1), 173–195.

JORDAN, P., JAUNET, V., TOWNE, A., CAVALIERI, AÉ V.G., COLONIUS, T., SCHMIDT, O. & AGARWAL, A. 2018 Jet–flap interaction tones. *J. Fluid Mech.* **853**, 333–358.

KAMBE, T., MINOTA, T. & IKUSHIMA, Y. 1985 Acoustic wave emitted by a vortex ring passing near the edge of a half-plane. *J. Fluid Mech.* **155**, 77–103.

LEE, S., AYTON, L., BERTAGNOLIO, F., MOREAU, S., CHONG, T.P. & JOSEPH, P. 2021 Turbulent boundary layer trailing-edge noise: theory, computation, experiment, and application. *Prog. Aerosp. Sci.* **126**, 100737.

LIGHTHILL, M.J. 1952 On sound generated aerodynamically i. General theory. *Proc. R. Soc. Lond. A: Math. Phys. Sci.* **211**, 564–587.

MACDONALD, H.M. 1915 A class of diffraction problems. *Proc. Lond. Math. Soc.* **2** (1), 410–427.

MENOUNOU, P. & NIKOLAOU, P. 2017 Analytical model for predicting edge diffraction in the time domain. *J. Acoust. Soc. Am.* **142** (6), 3580–3592.

MENOUNOU, P., SPIROPOULOS, M.I. & NIKOLAOU, P. 2023 Approximate time domain solution for studying infinite wedge diffraction, its parameters, and characteristics. *J. Acoust. Soc. Am.* **153** (2), 1399–1411.

MOREAU, D.J. & DOOLAN, C.J. 2013 Noise-reduction mechanism of a flat-plate serrated trailing edge. *AIAA J.* **51** (10), 2513–2522.

MOREAU, S. & ROGER, M. 2009 Back-scattering correction and further extensions of Amiet's trailing-edge noise model. Part II: application. *J. Sound Vib.* **323** (1), 397–425.

OBERHETTINGER, F. 2012 *Tables of Fourier Transforms and Fourier Transforms of Distributions*. Springer Science & Business Media.

POWELL, A. 1964 Theory of vortex sound. *J. Acoust. Soc. Am.* **36** (1), 177–195.

PRIDDIN, M., BAKER, D.I., AYTON, L.J. & PEAKE, N. 2018 Vortex sound models: passive and active noise control. In 2018 AIAA/CEAS Aeroacoustics Conference, pp. 3298.

PRINJA, R., JORDAN, P. & MARGNAT, F. 2025 Experimentally informed, linear mean-field modelling of circular cylinder aeroacoustics. *Theor. Comput. Fluid Dyn.* **39** (2), 1–33.

https://doi.org/10.1017/jfm.2025.10580 Published online by Cambridge University Press

ROGER, M. & MOREAU, S. 2005 Back-scattering correction and further extensions of Amiet's trailing-edge noise model. Part 1: theory. *J. Sound Vib.* **286** (3), 477–506.

ROGER, M., MOREAU, S. & KUCUKCOSKUN, K. 2016 On sound scattering by rigid edges and wedges in a flow, with applications to high-lift device aeroacoustics. *J. Sound Vib.* **362**, 252–275.

SANO, A., ABREU, L.I., CAVALIERI, A.V.G. & WOLF, W.R. 2019 Trailing-edge noise from the scattering of spanwise-coherent structures. *Phys. Rev. Fluids* **4** (9), 094602.

STOFFEL, A., MARGNAT, F., PRAX, C. & VANHERPE, F. 2025 Whistling side-view mirrors: modelling ladder-type structure tonal noise from flow intermittency. *J. Sound Vib.* **601**, 118919.

TIOMKIN, S. & JAWORSKI, J.W. 2024 Revisiting the frozen gust assumption through the aeroacoustic scattering of wavepackets by a semi-infinite plate. *J. Sound Vib.* **571**, 117989.

WANG, M. & MOIN, P. 2000 Computation of trailing-edge flow and noise using large-Eddy simulation. *AIAA J.* **38** (12), 2201–2209.

YUAN, Z., DEMANGE, S., JEKOSCH, S., SARRADJ, E., OBERLEITHNER, K., CAVALIERI, A.V.G. & HANIFI, A. 2024 Wavepackets driving trailing edge noise. Part i–direct simulation and experiments. In 30th AIAA/CEAS Aeroacoustics Conference (2024), pp. 3123.

https://doi.org/10.1017/jfm.2025.10580 Published online by Cambridge University Press